Percolation behaviors of ionic and electronic transfers in Li 3–2x Co x N

J.-C. Badot, E. Panabiere, N. Emery, Olivier Dubrunfaut, S. Bach, J.-P. Pereira-Ramos

Percolation behaviors of ionic and electronic transfers in $Li_{3-2x}Co_xN$

J.C. Badot *[1,4], E. Panabière [2], N. Emery [2], O. Dubrunfaut [3],
S. Bach [2], and J.P. Pereira-Ramos [2]

[1] *Chimie ParisTech, PSL Universté Paris, CNRS,*
Institut de Recherche de Chimie Paris, 75005 Paris, France
[2] *Institut de Chimie et des Matériaux Paris-Est, CNRS, Groupe d'Electrochimie et Spectroscopie des Matériaux (GESMAT), 2-8, rue Henri Dunant - 94320 Thiais, France*
[3] *GeePs Group of Electrical Engineering - Paris, UMR CNRS 8507, CentraleSupélec, Sorbonne Universités, Univ Paris-Sud, Université Paris-Saclay,*
11 rue Joliot-Curie, 91192 Gif-sur-Yvette, France
[4] *Réseau sur le Stockage Electrochimique de l'Energie (RS2E), FR CNRS 3459, France*
[5] *Université d'Evry Val d'Essonne, Dept Chimie, Bd F. Mitterrand, 91000 Evry*

* Corresponding author

Key words: Broadband Dielectric Spectroscopy; Lithium nitridocobaltate; Percolation; ionic and electronic conductivity

Abstract

Nitridocobaltates $Li_{3-2x}Co_xN$, with Li_3N-type layered structure, are promising compounds as negative electrode materials for Li-ion batteries. In the present paper, we report the first detailed broadband dielectric spectroscopy (BDS) study on lithiated transition metal nitrides. Ionic and electronic conductivities of $Li_{3-2x}Co_x\square_xN$ compounds ($0 \leq x \leq 0.44$) are investigated as a function of the concentration *x* of cobalt ions, cationic vacancies (□) and lithium ions. Dielectric and conductivity spectra were recorded within the frequency range 60 - 10^{10} Hz from 200 to 300 K. Experimental results exhibit two types of electric conduction: the first one is due to lithium ion diffusion (for $0 \leq x \leq 0.25$) and the second one to electronic transfers (for $x \geq 0.3$). Furthermore, two percolation transitions are evidenced and associated with 3D ionic transfers (threshold at $x \approx 0.11$) on the one hand and 2D electronic transfers (threshold at $x \approx 0.30$) on the other hand. By increasing the frequency, dielectric relaxations appear from larger to smaller sample scales. These successive polarizations appear with increasing frequency according to the following order: (a) sample/silver paint interface; (b) particles (aggregates of grains); (c) grains (crystallites); (d) local ionic and electronic motions within the grains. Evolutions of dielectric relaxation parameters (dielectric strength and relaxation frequency) with Co content confirm the two percolation transitions. Surprisingly, the grain conductivity has a large discontinuity immediately below the electronic percolation threshold where any local- and long-range ionic movement disappears without electronic transfer. This discontinuity would be due to a narrow transition from ionic to electronic conduction when x increases.

1. Introduction

In the last few years, various transition metal compounds in Group V (nitrides [1,2], phosphides [3,4] and antimonides [5,6]) have been investigated as negative electrode materials according to either conversion or insertion reactions for Li-ion batteries. Among nitrides, ternary lamellar compounds with general formula $Li_{3-x}M_xN$ (M = Co, Ni, Cu) and 3D antifluorite-type compounds such as Li_7MnN_4 or Li_3FeN_2 have attracted great interest due to their reversible Li insertion properties [1,2,7,8,9,10,11,12]. After pioneering works by Japanese groups showing the potential interest of 2D-nitrides through conversion reactions [13,14], we have recently deeply reinvestigated the structural and electrochemical properties of Li-Co-N and Li-Ni-N systems. These compounds were identified as the most promising 2D-nitrides [15,16,17,18]. Nitridocobaltates compounds, obtained using a solid state route from various mixture of Li_3N and Co metal heat-treated at 700°C in a nitrogen gas stream have a general formula $Li_{3-2x}Co_x\square_xN$ ($0 \leq x \leq 0.44$). In this solid-solution system, an equivalent amount *x* of Co^{2+} ions and lithium vacancies □, leads to a smooth and continuous evolution of the cell parameters versus the cobalt content, according to the Vegard's law [16,19]. Also, in the reduced potential window 0.02-1V vs Li^+/Li, our group demonstrated that these materials are also the first example of intercalation compounds based on a layered nitrogen framework [16,17]. An excellent cycle life is achieved with a stable specific capacity of 180 mAh g^{-1} at C/5 for $Li_{2.12}Co_{0.44}\square_{0.44}N$. Its electrochemical fingerprint is characterized by a single step around 0.6 V, consistent with the Co^{2+} ions content and a lithium accommodation occurring in the cationic vacancies (□) located in Li_2N^- layers. As a consequence, from a structural point of view, the hexagonal layered structure is maintained with a negligible strain limited to a volume expansion of only 1% upon the discharge-charge process. This mechanism explains the excellent cycling life of these $Li_{3-2x}Co_x\square_xN$($0 \leq x \leq 0.44$) nitrides where the Co^{2+}/Co^+ redox couple, lithium ions and cationic vacancies govern

the electrochemical features. Therefore, a better knowledge of electronic and ionic transports would help to understand their physical properties.

Due to the widely different time scales related to ionic and electronic diffusion in electrode materials, electrochemical methods are appropriate to characterize ionic diffusion properties while electron motion properties cannot be described with these techniques. Conversely, the broadband dielectric spectroscopy from a few Hz to microwave frequencies (a few GHz) is a powerful technique allowing the electrical parameters like permittivity, resistivity and conductivity to be determined as a function of frequency. Such a spectroscopy has been already applied to a multiscale description of electronic transport in various cathode materials for Li-ion batteries like Li_xMoO_3, Li_xFePO_4, $Li_{1+x}V_3O_8$ composite electrodes [20,21,22,23]. These previous papers have shown that the BDS data cannot be analyzed and interpreted without a thorough knowledge of the material under study (composition, crystal structure, microstructure,…).

Li_3N exhibits a layered structure and is well-known for its ionic conductivity within the Li_2N^- planes, with a conductivity value of $\sigma = 10^{-1}$ S m^{-1} [24,25]. Considering the $Li_{3-2x}Co_xN$ solid-solution system, with the same layered host lattice than Li_3N, remarkable properties of ionic conduction are expected. Indeed, the increasing amount of lithium vacancies with the cobalt content is expected to be favorable to the ionic conductivity while the introduction of cobalt ions in the structure is favorable to a better electronic conduction, eventually by localized electrons movements through these compounds.

In the present paper, we report the first detailed BDS study on transition metal nitrides to investigate ionic and electronic conductivities in the solid-solution system $Li_{3-2x}Co_xN$ ($0 < x < 0.44$) as a function of the Co ions, cationic vacancies and lithium ions concentration.

2. Experimental

2.1. Synthesis and structure

$Li_{3-2x}Co_xN$ samples were synthesized through a solid-state route under nitrogen flux. To prepare various compositions of the solid solution $Li_{3-2x}Co_xN$, several mixtures of Li_3N and Co powders were thoroughly ground in an agate mortar and then pressed into pellets. The pellet of about 1 g was then transferred in an alumina crucible enclosed in a tubular stainless steel reactor and heated during 8 h at 720°C under a nitrogen gas stream. A second alumina boat filled with titanium sponge was also added to trap any oxygen and moisture traces present in the gas. All manipulations were carried out in an argon glove box. The Li_3N sample is obtained after a thermal treatment under nitrogen of a pellet made with commercial Li_3N powder. This step is mandatory to have a straight comparison with samples of the Co-contained solid-solution system since the commercial powder contains the two structural polymorphs (α and β) of Li_3N. After the annealing at 720°C under nitrogen gas stream, only the α polymorph (P6/mmm space group) is obtain. X-ray diffraction patterns of the as prepared powder were performed using a Panalytical X'pert pro diffractometer equipped with a Co Kα source and an X'celerator detector. Due to the air sensitive character of these nitrides, a polymer airtight sample holder was used.

2.2. Broadband dielectric spectroscopy

Complex permittivity and conductivity of $Li_{3-2x}Co_xN$ samples were measured by the broadband dielectric spectroscopy (hereafter called BDS) from 60 to 10^{10} Hz, using simultaneously a network analyzer Agilent PNA E8364B (10^7 to 10^{10} Hz), two impedance analyzers Agilent 4294 (60 to 1.1_x10^8 Hz) and Agilent 4291 (10^6 to 1.8_x10^9 Hz). The experimental device consists of a coaxial cell (APC7 standard), in which the cylindrically shaped sample (metallized powder pellet with diameter = 3 mm and thickness ≈ 1 mm) fills the gap between the inner conductor and a short-circuit [20,21,26] (Figure S1). After a

relevant calibration of the analyzers, the sample admittance Y_s is measured. The knowledge of Y_s allows determining the complex (relative) permittivity $\varepsilon(\omega) = \varepsilon'(\omega) - i\varepsilon''(\omega)$ of the sample, which enables the calculation of the complex resistivity $\rho(\omega) = [i\omega\varepsilon_0\varepsilon(\omega)]^{-1}$ (ε_0 being the vacuum permittivity) and conductivity $\sigma(\omega) = [\rho(\omega)]^{-1}$ whose real part $\sigma'(\omega)$ will be hereafter called the frequency dependent conductivity. Before the measurements of the sample, a calibration process is applied to remove the systematic errors of the analyzers and coaxial guide. Complete dielectric spectra have been made from about 600 measurements with an accuracy of approximately 3 to 5%.

3. Results and discussion

3.1. Structure and microstructure

XRD patterns of $Li_{3-2x}Co_xN$ samples are displayed in Fig. 1a and 1b. These data can be easily indexed using a hexagonal structure isotype of α–Li_3N (space group P6/mmm) and all the cell parameters are gathered in Fig. 1c and Table 1. Such a structure (Fig. 1d) can be simply described by a hexagonal nitrogen network where N^{3-} ions (*1a* site) are surrounded by 6 Li^+ ions (*2c* site), forming Li_2N^- layers. A Li^+ layer (*1b* site) separates these layers. Finally, N^{3-} ions are arranged in the center of edged sharing hexagonal bipyramids of Li^+ ions. When Co^{2+} ions substitute a fraction of Li^+, it occupies the *1b* site, i.e. the cationic interlayer plane and an equivalent amount of vacancies is created in the *2c* plane, i.e. in the Li_2N^- plane. Lithium ions of *1b* and *2c* sites will be hereafter called $Li^+(1b)$ and $Li^+(2c)$, respectively. The partial substitution of lithium by cobalt induces changes in electrostatic interaction between plans. Indeed, the integration of Co^{2+} in the pure Li^+ layer increases its overall positive charge while the creation of cationic vacancies in the Li_2N^- plane rises the global negative charge. Consequently, the interlayer distance that is directly related to the *c* axis parameter, decreases linearly with the augmentation of Co^{2+} content, from c = 3.876(8) Å for Li_3N to c = 3.625(7) Å for $Li_{2.12}Co_{0.44}N$ (Fig. 1c). The *a* parameter gradually increases with the cobalt content, from a

= 3.667(7) Å for Li_3N to a = 3.730(7) Å for $Li_{2.12}Co_{0.44}N$, probably due to the progressive reduction of the screening effect of lithium ions between neighboring nitrogen ions. As a result, $Li_{3-2x}Co_xN$ compounds follow the Vegard's law since *a* and *c* parameters vary linearly with cobalt substitution (Fig. 1c). Cells parameters of Li_3N and of $Li_{2.12}Co_{0.44}N$ well agreed with previous reports (ref [27,28] and [16,29] respectively). Despite all the precautions taken during the synthesis procedure, a small Li_2O impurity is present on XRD patterns. However, due to the selective character of the BDS and the insulating nature of the Li_2O, the impurity does not affect the measurements.

Scanning Electron Microscopy (SEM) micrograph (Fig. 1e) shows the microstructure of the powder, which is constituted of large aggregates with an average size of about 15 to 20 μm. Furthermore, the aggregates are made of smaller particles (or grains) with an average size of about 1 to 3 μm (Fig. 1e).

3.2. Conductivity and permittivity: long-range and local ionic and electronic motions

Conductivity and permittivity spectra (ε' and σ' vs. frequency ν) of the different samples at room temperature are shown in Figure 2. Whatever the sample and the temperature in the 200-300 K range, the real part of the conductivity σ' (Fig. 2a) increases up to more than five orders of magnitude over the frequency range 60 to 10^{10} Hz. On the contrary, related real parts of the permittivity ε' (Fig. 2b) decrease by about four orders of magnitude in the same frequency range. Also, real parts ε' and σ' are highly dependent on the cobalt content x and show several knocks due to various dielectric relaxations. Nevertheless, the frequency-dependent representation does not permit to distinguish easily these different relaxations. The complex plane representation (Nyquist plot) is more convenient to decompose the electric spectra into different contributions.

Nyquist plots of the complex resistivity (or impedance) are better adapted to the determination of the resistivity and the conductivity at the different scales of the materials (sample, aggregates of grains, and grains within the aggregates). Samples complex resistivity is generally described by series combination of impedances, each one being parallel combination of a capacitor and a resistor related to the effective permittivity and conductivity at a given scale of the material. Hence, the total resistivity of a conducting material is the sum of various contributions (relaxation functions) given by Equation 1 [30]:

$$\rho(\omega) = \rho_g + \left[\sum_m \frac{\Delta\rho_m}{1+ (i\omega\tau_{\rho m})^{1-\alpha_m}}\right] \quad (1)$$

where $\omega = 2\pi\nu$ is the angular frequency (in s^{-1}) and ρ_g the intrinsic dc-resistivity (inverse of the dc conductivity σ_g) of the grain. The term in brackets of Eq. 1 is the sum of the complex resistivities associated to each scale of the sample from macroscopic to interatomic size. $\Delta\rho_m$ corresponds to the resistance of each junction (silver paste/sample, aggregate/aggregate and grain/grain) of the sample, τ_m is a mean relaxation time and α_m a fitting parameter ($0 \leq \alpha_m \leq 1$). Equation 1 is valid only at the frequencies for which the real part of $\rho(\omega)$ is higher than ρ_g (dc-resistivity of the grain). In this condition, low and high frequency parts of $\rho(\omega)$ have the same origin since they are due to charge transfers at the different scales of the materials (sample, aggregates of grains, and grains within the aggregates). In Nyquist plot representation, each component is plotted by a circular arc more or less centered below the ρ' axis. This representation aims at determining the intrinsic grain resistivity ρ_g and the conductivity σ_g. Since the impedances at different scales are additive (cf. Eq. 1), their contributions are obtained by a decomposition procedure of the resistivity spectra. In some cases, Nyquist plots of conductivity are more suitable, if the decomposition procedure of the spectra into different components is not easy from complex resistivity plots. Validity of Equation 1 is limited to the frequency range where the real part of $\rho(\omega)$ is higher

than ρ_g (dc-resistivity of the grain). In this condition, low and high frequency parts of $\rho(\omega)$ are the same origin since they are due to charge transfers at the different scales of the materials (sample, aggregates of grains, and grains within the aggregates). However, local mechanisms (electronic and ionic local motions within the grain), which occur at the high-frequency part of the spectrum, are analyzed more precisely using Nyquist plots of complex permittivity. The Nyquist plots of complex resistivity for $Li_{2.76}Co_{0.12}N$ and $Li_{2.22}Co_{0.39}N$ at room temperature are shown in Fig. 3a and b, respectively. First, two relaxations R1 and R2 are evidenced. The high frequency contribution R2 is determined by subtracting the low frequency contribution R1 of the total resistivity. The R1 relaxation results in the existence of inter-particle contact resistances and capacitances. The R2 relaxation is thus due to contact resistances and capacitances at grain (crystallite) boundaries inside the particles (aggregates). The high frequency part of R2 crosses the ρ' axis at $\rho' = \sigma_g^{-1}$ where σ_g is the conductivity of the grain or crystallite. Moreover, an additional contribution occurs at frequencies lower than 10^3 Hz for $Li_{2.76}Co_{0.12}N$ (Fig. 3a). The latter corresponds to the contact resistance and capacitance of the interface between the sample and silver metallization. This phenomenon is typical of a metal/ionic conductor junction, giving rise to ionic double-layer at the sample surface. As shown in Fig. S2, conductivity Nyquist plots have been used to determine precisely grain conductivities of Li_3N, $Li_{2.90}Co_{0.05}N$ and $Li_{2.64}Co_{0.18}N$. The different values of the grain conductivities at room temperature are summarized in Table 2. Fig.4 plots the grain conductivity σ_g in function of x (i.e. molar contents of lithium vacancies and Cobalt) at room temperature. The grain conductivity σ_g evolution presents a large discontinuity with a drop of a factor 4 when x varies from 0.25 to 0.32. Also, two well-separated conductivity regimes are thus evidenced in Fig. 4 and due to two types of charge carriers (lithium ions and electrons). They are associated with ionic transfers for lower cobalt contents ($0 \leq x \leq 0.25$) and to electronic transfers for higher cobalt contents (for $0.32 \leq x \leq 0.44$). Electronic transfer only

occurs in a 2D continuous network of cobalt ions between Co ions. This finding suggests the presence of a small amount of Co^{+} ions. Evolutions of ionic and electronic conductivities with the temperature provide information on the activation energies of both types of conductivity. Indeed, as demonstrated theoretically, the temperature dependence of ionic conductivity σ_{gi} is given by:

$$\sigma_{gi} = \frac{A}{T} exp\left(-\frac{E_{gi}}{kT}\right) \quad (5)$$

as shown in Fig. 5a for x = 0, 0.05, 0.12, 0.18 and 0.25. A is a conductivity prefactor, T the temperature, k the Boltzmann constant and E_{gi} the activation energy with values between 0.19 and 0.21 eV (see Table 2). For localized electron system like ionic compounds, electronic transport is usually given by [31,32]

$$\sigma_{ge} = \sigma_{0e} exp\left(-\frac{E_{ge}}{kT}\right) \quad (6)$$

as shown in Fig. 5b for x = 0.32, 0.39 and 0.44. The activation energy is $E_{ge} = E_m - E_F$, where E_m and E_F are the mobility edge energy (bottom of the conduction band) and the energy at Fermi level, respectively. σ_{0e} is the conductivity prefactor (local conductivity), E_{ge} the activation energy with values between 0.19 and 0.23 eV (see Table 2). σ_{oe} is not temperature dependent since electrons move by means of transitions between nearest neighbor cobalt ions. Then their local mobility follows the Einstein relation [32],

$$\mu \propto \frac{ea^2}{kT}\ 2\pi\nu_t \quad (7)$$

where ν_t is the transfer frequency (independent of the temperature) between nearest neighbors cobalt ions, *e* the electron charge and *a* the distance between them. The local conductivity σ_{0e} is defined as the product of the density of states by the mobility m. Consequently, σ_{0e} is temperature independent since the density of states is proportional to kT in 2D semiconductors, which confirm the Arrhenius plot of Fig 5b. Previous work on $LiNi_{1/3}Mn_{1/3}Co_{1/3}O_2$ exhibits a similar character [33]. ~~In summary, the activation energies of~~

~~ionic and electronic conductivities of the grain are similar, because lithium cations and electrons would feel the same Coulombic interactions within the crystal lattice.~~

Nyquist plots of the complex permittivity distinguish the responses of the electric polarizations within the samples. It allows to determine their relaxation strengths and frequencies related to both charge mobility and to the existence of interfaces at the different levels of the samples. The interfaces give rise to space-charge relaxations in the lower frequency range of dielectric spectra. On the other hand, relaxations due to fast local charge motions are often observed in the higher frequency range of the same spectra. In the considered frequency range, the frequency dependent complex permittivity is generally given by:

$$\varepsilon(\omega) = \varepsilon_{lat} + \left\{ \sum_j \frac{\Delta\varepsilon_j}{\left[1+(i\omega\tau_j)^{1-\alpha_j}\right]^{\beta_j}} \right\} + A(i\omega)^{s-1} + \frac{\sigma_s}{i\omega\varepsilon_0} \quad (7)$$

where ε_{lat} is the lattice permittivity of the grain (crystallite), σ_s the dc-conductivity of the sample, $\varepsilon_0 = 8.842\times10^{-12}$ F.m^{-1} the vacuum permittivity, and s an empirical parameter ($0 \leq s \leq 1$). The term in curly brackets is the sum of Havriliak-Negami (or HN) relaxation functions with fitting parameters $0 \leq \alpha_j \leq 1$ and $0 \leq \beta_j \leq 1$. For $\beta_j = 1$ (i.e. Cole-Cole or CC function), the Nyquist plot of such relaxation is a circular arc centered under ε' axis whereas it is a skewed arc for $\alpha_j = 0$ (Cole-Davidson or CD function). $\Delta\varepsilon_j$ is the dielectric strength and τ_j the mean relaxation time corresponding to relaxation frequency $\nu_j = (2\pi\tau_j)^{-1}$. The term $A(i\omega)^{s-1}$ with $0 \leq s \leq 1$ can be observed in the low-frequency range for disordered conducting networks at the macroscopic (sample) scale or to distributions of contact resistances and capacitance between metallization and the sample. The Nyquist plot of such behavior is a straight line whose angle $\theta = (1-s)\pi/2$ with the ε'-axis is the smaller as the parameter s is higher: the straight line is vertical for $s = 0$ and merged with the sample dc-conductivity σ_s. The relaxations can be evidenced by a decomposition procedure of dielectric spectra due to the additivity of

polarizations at the different scales of the sample. Hence, the decomposition procedure of a spectrum is made by successive subtractions of the contributions starting from lower to higher frequencies. The entire Nyquist plots show that the low-frequency parts of the spectrum are well fitted by straight lines (contributions P1) corresponding to the power-law term $A(i\omega)^{s-1}$ (Fig. 6-8, Fig. S4-S7 and Table S1). Experimental data show that the parameter s is between 0 and 0.06 for all the samples except Li_3N and $Li_{2.90}Co_{0.05}N$ where s = 0.30 and 0.4 respectively. Less conductive samples (Li_3N and $Li_{2.90}Co_{0.05}N$) have few mobile charge carriers (Li^+), due to a random distribution of lithium vacancies in the conducting planes. The resulting distribution of diffusion lengths increases the tortuosity of the ionic 2D conduction network in Li_3N and $Li_{2.90}Co_{0.05}N$. On the contrary, P1 contributions of the most conductive samples ($Li_{3-2x}Co_xN$ with $0.12 < x < 0.44$) are quasi-merged with that of sample dc-conductivities showing narrow distributions of ionic diffusion lengths. The decomposition procedure of a dielectric spectrum is performed as follows: a) the P2 relaxation is evidenced after subtraction of the P1contribution; b) the relaxations P3, P4, P5 and P6 are obtained after subtractions of P2, P3, P4 and P5, respectively. Five relaxations are evidenced for the ionic conductors ($Li_{2.90}Co_{0.05}N$ to $Li_{2.50}Co_{0.25}N$) while there are only four for α-Li_3N and the electronic conductors ($Li_{2.36}Co_{0.32}N$ to $Li_{2.12}Co_{0.44}N$). Fig. 6-8) show the permittivity Nyquist plots at room temperature of $Li_{2.64}Co_{0.18}N$ (ionic conductor), $Li_{2.36}Co_{0.32}N$ (low electronic conductor) and $Li_{2.22}Co_{0.39}N$ (good electronic conductor), respectively (see Table 2). The Nyquist plots of other samples are described in Supporting Information (Fig. S1-S5). The P2, P3 and P4 dielectric relaxations are due to polarization fluctuations at different scales of the sample. Their corresponding relaxation frequencies are ν_2, ν_3 and ν_4, respectively. The first one P2 is attributed to Ag/sample interface giving rise to a space-charge polarization at sample scale. The two others P3 and P4 correspond to the relaxations of the space-charge polarizations of the particles (aggregates of grains) and the grains, respectively. The existence

of space-charges are the result of accumulated electrons and lithium ions at particle and grain surfaces. Relaxation frequencies and dielectric strengths of the three different types of space-charge polarizations are summarized in Fig. S4-7 and Table S2 of Supporting Information. Considering all the studied samples, the relaxation frequencies ν_2, ν_3 and ν_4 are in the following frequency ranges at room temperature: a) $10^2 < \nu_2 < 3\times10^5$ Hz for the silver paste/sample contribution, b) $6.3\times10^4 < \nu_3 < 7\times10^7$ Hz for the particle contribution and c) $1.3\times10^7 < \nu_4 < 3.9\times10^8$ Hz for the grain contribution (Fig. S4-7 and Table S2). Note, that the space-charge relaxation following grain polarization (P4) is mainly due to bound charges (Li+ and electrons) at grain surface. Hence, when a grain is submitted to an electric field, charges are un-trapped from the grain boundary, move through the grain core and tend to be accumulated on the opposite boundary side. This type of motion needs more activation energy to perform the transfer, i.e. $E_g > E_i$ or $E_g > E_e$ (Table 2 and S2). The higher frequency contributions P5 and P6 are thus due to polarization fluctuations within the grain. They are the consequence of the intrinsic local motions of electrons and lithium ions which are observed in the samples. The relaxations P5 and P6 are both observed only for the ionic conductors $Li_{3-2x}Co_xN$ with $0.05 \leq x \leq 0.25$. As P5 relaxation is only present for α-Li_3N, which is a pure ionic conductor, it allows us to attribute this relaxation to a local Li^+ hopping in the *ab* plane of the Li_3N structure. The Li^+ hopping is only possible if there is a contiguous lithium vacancy, i.e. the existence of at least one Li^+-vacancy pair. According to [24,25], some vacancies are present in the sample due to small contaminations. Its characteristic frequency $\nu_i = 6\times10^8$ Hz at room temperature (Table 2) follows the Arrhenius law with an activation energy of about 0.19 eV and a prefactor $\nu_{0i} = 9\times10^{11}$ Hz. For samples $Li_{2.90}Co_{0.05}N$, $Li_{2.76}Co_{0.12}N$ and $Li_{2.64}Co_{0.18}N$, P5 relaxations have characteristic frequencies of the same order of magnitude than that of Li_3N with similar activation energies E_i between 0.19 and 0.20 eV (Fig.9a and Table 2) and prefactors ν_{0i} between 9.0×10^{11} and 1.1×10^{12} Hz (Fig. 9a

and Table 2). For samples $Li_{2.90}Co_{0.05}N$ to $Li_{2.64}Co_{0.18}N$ (electronic insulators), the P6 relaxation is due to the fast motion of the electrons on isolated cobalt clusters with characteristic frequencies ν_e ranking between 2.7×10^9 and 3.7×10^9 Hz at room temperature (Fig. 9b and Table 2). These frequencies ν_e are also thermally activated, with activation energies E_e of about 0.18 - 0.20 eV (Fig. 9a-c) and prefactors ν_{0e} in the range 3×10^{12} - 4×10^{12} Hz (Table 2). The ionic conductor $Li_{2.50}Co_{0.25}N$ is a special case, because the relaxation frequency of P5 attributed to Li^+ motion ($\nu_i = 10^{10}$ Hz with $E_i = 0.19$ eV), is higher than P6 relaxation frequencies, attributed to electrons$^-$ in Co clusters ($\nu_e = 1.2\times10^9$ Hz with $E_e = 0.25$ eV) (Fig. 9b) and Table 2). As the activation energy of the local motion must be less than or equal to that of the grain conductivity (i.e. $E_g = 0.21$ eV), the attributions of P5 and P6 are thus justified for $Li_{2.50}Co_{0.25}N$. Indeed, based on the conductivity analysis, which indicates the ionic nature of $Li_{2.50}Co_{0.25}N$ conduction, and the lower activation energy of P5 relaxation regards the grain activation energy E_g, the Li^+ ionic motion is ascribed to the highest relaxation frequency (with $\nu_i = 10^{10}$ Hz). For electronic conductors ($Li_{2.36}Co_{0.32}N$, $Li_{2.22}Co_{0.39}N$ and $Li_{2.12}Co_{0.44}N$), only local electronic motions corresponding to P6 are observed (Fig. 7, 8) and S7). Frequencies ν_e are thermally activated with activation energies E_e of about 0.18-0.20 eV (Fig. 9c) and prefactors ν_{0e} in the range $6\times10^{11} – 4.6\times10^{12}$ Hz (Table 2). The P6 relaxation is fitted by Debye functions for $Li_{2.22}Co_{0.39}N$ and $Li_{2.12}Co_{0.44}N$, and by a CD-function for $Li_{2.36}Co_{0.32}N$ (Fig. 7) and Table 2). Relaxation frequencies (ν_i and ν_e) and dielectric strengths ($\Delta\varepsilon_i$ and $\Delta\varepsilon_e$) for ion and electron motions are respectively minimum and maximum as a function of x (Fig. 9 d and e). The origin of these behaviors will be fully developed in the next section.

3.3. Origin of ionic and electronic conductivities: evidence of percolations in $Li_{3-2x}Co_xN$

Like for the grain conductivities, the activation energies of the relaxation frequencies ν_i and ν_e are similar because ions and electrons undergo the same attractive electrostatic interactions to move through the crystal lattice (Table 2). The following expression [34,35],

$$\frac{\sigma_g}{2\pi p \varepsilon_0 \Delta\varepsilon_k} = \nu_k \quad (8)$$

shows that the experimental findings described in Fig. 10 are well fitted with the correlation factor $p \approx 1$. Here σ_g is the grain conductivity, $\Delta\varepsilon_k$ the dielectric relaxation strength and ν_k the relaxation frequency where the subscript *k* corresponds to *i* for ionic conductors and to *e* for electronic conductors (see Table 2). Consequently, inner grain conduction and local polarization have the same origin in $Li_{3-2x}Co_xN$, whatever the type of charge carrier (electron or ion). Fig. 4 shows significant rises of ionic and electronic conductivities for x above 0.11 and 0.30, respectively. Dielectric strengths ($\Delta\varepsilon_5$ and $\Delta\varepsilon_6$) and relaxation frequencies (ν_5 and ν_6) exhibit critical behaviors near of the same x contents. These behaviors can be likened to percolation transitions according to the predictive percolation models on conductivity, permittivity and relaxation frequency [36,37,38,39,40,41] (see Supporting Information S4). Furthermore, the CD function, which fits the relaxation P6 in $Li_{2.36}Co_{0.32}N$ (i.e. x = 0.32) (Fig. 7) is justified by previous computational and theoretical models for systems slightly above of the percolation threshold [42,43].

Fig. 11a and b show the distribution of cobalt ions in the crystal lattice perpendicular to c-axis for x = 0.18 and x = 0.44, respectively. As the Co^{2+} cations substitute Li^+ cations in the *1b* sites (interlayer space), the electronic transfer is expected to occur only in the two-dimensional triangular lattice formed in the *ab* plane for $x > x_{ce} \approx 0.30$ (Fig. 11b). Then, a 2D continuous network of cobalt ions appears which facilitates electronic transfers between Co ions. This finding suggests the presence of a small amount of Co^+ ions. For x > 0.30 and outside the critical region (i.e. x = 0.39 and 0.44), the experimental data can be fitted by a

straight line which is described by the expression of the effective medium approximation for bond percolation (EMA theory [40,41]:

$$\sigma_{ge} = \sigma_m \left[\frac{z}{z-2}x - \frac{2}{z-2}\right] \quad (2)$$

where σ_{ge} is the grain electronic conductivity, a fitting parameter $\sigma_m \approx 18$ S m^{-1} (i.e. maximum electronic conductivity) and z = 6.06, the cobalt coordination number. This result is in good agreement with observed 2D bond percolation in our triangular lattice (z = 6 and $x_{ce} \approx$ 0.33).

On the contrary, Li^+ diffusion can have a three-dimensional character, especially for some x values as discussed below. Indeed, since the percolation thresholds on 2D networks are higher than those of 3D networks, the second threshold at $x_{ci} \approx 0.10$ - 0.12 corresponds to a 3D percolation of the ionic conductivity σ_{gi} of $Li_{3-2x}Co_xN$ grains. The rise of the ionic conductivity is here due to the increase of the number of lithium vacancies and thus, to Li^+ motions. For x < 0.11, Li^+(*2c*) ions only diffuse in *ab* planes thanks to the presence of a limited number of lithium vacancies. The lithium diffusion mechanism is then expected to be similar to the diffusion process encountered in Li_3N, where the Li^+ conductivity was explained by the presence of 1 or 2% of lithium vacancies due to structural defects or hydrogen contamination [44]. Since for x < 0.11, the number of lithium vacancies induced by the limited amount of Co^{2+} present in the structure, similar diffusion paths are expected with conductivity of same order of magnitude. For 0.11 < x < 0.25, the number of lithium vacancies is such that Li^+(*2c*) ions, i.e. Li ions in the $Li_{2-x}N^-$ planes, might diffuse in both parallel directions to *ab* planes (in the $Li_{2-x}N^-$ planes) and also along the *c*-axis. However, for x between 0.25 and 0.32, the ionic conductivity drops to ~0, where the percolation of the electronic conductivity takes place (Fig. 4). It does not indicate the full disappearance of the ionic conductivity, only that the ionic conductivity becomes negligible regards to the true in-plane electronic contribution. Long-range motions of Li^+(*2c*), might be blocked along the c-

342 axis by the percolated network of the cobalt ions, which leads to strong electrostatic
343 repulsions. The ionic conductivity should come back to a 2D regime within the layer (2c site),
344 with more space for Li^+ transport via vacancies (increasing content with x). However, Li(2c)
345 has an increasing number of nearest Co^{2+} neighbor on 1b sites in surrounding layers (upper
346 and lower, Fig. 1d and Fig. 11b). As the repulsive coulombic interactions between Li^+(2c) and
347 Co^{2+}(1b) for $x > 0.30$ are higher than those between Li^+(2c) and Co^{2+}(1b) for $x < 0.11$, the Li^+
348 (2c) transport should be slowed down. This results in a higher activation energy of the ionic
349 conductivity, which therefore, becomes smaller and thus negligible compared to the electronic
350 conductivity. Local polarizations attributed to ion local motion, are not detectable because
351 dielectric strengths $\Delta\varepsilon$ corresponding to their dielectric responses become small according to
352 the percolation theory (Supporting Information S4). Moreover, the plot of $\sigma_{gi} = f(x)$ does not
353 allow a full description of the 3D ionic percolation. The ionic conductivity σ_{gi} usually
354 depends on the mobile ions concentration whose mobility increases with the vacancies
355 concentration. It is then more suitable to represent the conductivity σ_{gi} as a function of $y = (2-x)x$, where (2-x) is the number of mobile Li^+(*2c*) and x the number of Li^+ vacancies in the *2c*
357 site of a single unit cell. The dependence of σ_{gi} with y is plotted in Figure 11c. A percolation
358 threshold at $y_{ci} = (2-x_{ci})x_{ci} \approx 0.23$ is suggested. Then, y_{ci} value is consistent with a 3D
359 percolation scheme with an ionic coordination number included between 8 and 12. In our
360 case, when considering the two layers surrounding the layer of the Li^+(*2c*) ion which will
361 diffuse, 11 possible neighboring sites are numbered: 3 in the same *ab* plane, as for the 2D
362 diffusion scheme observed for $x < 0.11$, and 4 sites per surrounding layer (Fig. 11d). Since
363 lithium diffusion is only possible if at least one of the neighboring sites is occupied by a
364 lithium vacancy, only a smooth increase of the conductivity at the percolation threshold y_{ci} is
365 evidenced according to a smooth transition from low to high conductivity behavior. In this
366 case, the ionic conductivity $\sigma_{gi}(y_{ci})$ at the percolation threshold is thus given by:

$$\sigma_{gi}(y_{ci}) = \sigma_L \left(\frac{\sigma_L}{\sigma_H}\right)^q \quad (3)$$

where σ_L is the ionic conductivity of Li_3N (*low electrical conductor*), σ_H the maximum ionic conductivity (*high electrical conductor*) that would be obtained at y = 1 and q ≈ 0.72 for a 3D conductor [45]. Since $\sigma(y_{ci}) \approx 0.5$ S m^{-1} and $\sigma_L = 0.1$ S m^{-1} at room temperature, the relation (3) gives $\sigma_H \approx 31$ S.m^{-1}. When $y > y_{ci}$, the conductivity increases with y as:

$$\sigma_{gi}(y) = \sigma_H \left(\frac{y-y_{ci}}{1-y_{ci}}\right)^t \quad (4)$$

where *t* is a critical parameter. Considering the conductivity values for y > 0.23 (or x > 0.12) and $\sigma_H = 31$ S.m^{-1}, Eq. 4 gives t = 1.6 for y = 0.33 (or x = 0.18) and t = 1.8 for y = 0.42 (or x = 0.24). This range of values of t is a suitable result for a 3D conductor given the margin of error.

Evolutions of grain conductivity and of dielectric relaxation parameters (dielectric strength and relaxation frequency) with Co content x confirm the two percolation transitions of ionic and electronic conductivities. The grain conductivity has a large discontinuity immediately below the electronic percolation threshold where any local- and long-range ionic movement become progressively negligible without electronic transfer. This discontinuity would be due to a narrow transition from ionic to electronic conduction when x increases.

4. Conclusion

For the first time, broadband dielectric spectroscopy from 60 to 10^{10} Hz has been applied to study both ionic and electronic transport properties of $Li_{3-2x}Co_xN$ solid-solution compounds. It has been possible using BDS to discriminate all the contributions of the conductivity. These successive relaxations appear with increasing frequency according to the following order: (a) sample/silver paint interface; (b) particles (aggregates of grains); (c) grains (crystallites); (d) local ionic and electronic motions within the grains. Complex plane plots of resistivity, conductivity and permittivity are thus used to determine grain (or intrinsic) conductivity and

391 to evidence dielectric relaxations at different scales of the samples from low to microwave
392 frequency range. Surprisingly, even if the structural parameters evolve linearly with the cobalt
393 content, three different conduction regimes are evidenced, separated by two percolation
394 transitions. The first percolation threshold, at $x \approx 0.11$, is associated to a transition from 2D to
395 3D ionic conduction regimes. This ionic conductivity increases significantly after the
396 percolation threshold of more than an order of magnitude to reach $\sigma_{gi} \approx 2.6$ S m^{-1} at room
397 temperature. Then, the second threshold at $x \approx 0.30$, results from the percolation of the Co
398 ions leading to continuous 2D electronic conductive network. The electronic conductivity
399 reaches an effective value close to $\sigma_{ge} \approx 3$ S m^{-1} for the highest cobalt content at room
400 temperature. In reality, the true 2D electronic conductivity is higher than its effective value
401 σ_{ge}, which is measured in a 3D isotropic sample. ~~Surprisingly, the both movements have~~
402 ~~similar activation energies ($0.19 eV < E_i < 0.21 eV$ and $0.19 eV < E_e < 0.23 eV$). This finding~~
403 ~~might be related to the existence of the same Coulomb interactions felt by the electrons and~~
404 ~~the lithium cations.~~ Moreover, ionic conduction becomes negligible beyond the electronic
405 percolation threshold ($x \approx 0.30$). The transport of lithium ions could be slowed by the
406 presence of a growing number of cobalt ions which creates strong electrostatic repulsions.
407 Experimental values of dielectric strengths and relaxation frequencies associated to the
408 intrinsic local ionic and electronic motions are well described by the percolation theory. The
409 present finding demonstrates the relevance of BDS analysis to discriminate the intrinsic
410 conductive properties of powdered samples.
411

412 **Table 1**. Composition, cell parameters and volume of the $Li_{3-2x}Co_xN$ solid-solution samples. The
413 composition were determined through Rietveld refinment of powder XRD data with the lithium
414 content fixed to 3-2x

Composition	a (Å)	c (Å)	Volume (Å^3)
Li_3N	3.667(7)	3.876(8)	45.1(2)
$Li_{2.90}Co_{0.05(2)}N$	3.669(7)	3.861(8)	45.0(2)
$Li_{2.76}Co_{0.12(2)}N$	3.678(7)	3.826(8)	44.8(2)
$Li_{2.64}Co_{0.18(2)}N$	3.687(7)	3.807(7)	44.8(2)
$Li_{2.50}Co_{0.25(2)}N$	3.692(7)	3.767(7)	44.5(2)
$Li_{2.36}Co_{0.32(2)}N$	3.712(7)	3.724(7)	44.4(2)
$Li_{2.22}Co_{0.39(2)}N$	3.716(7)	3.704(7)	44.2(2)
$Li_{2.12}Co_{0.44(2)}N$	3.730(7)	3.652(7)	44.0(2)

415

416

417

418

Table 2. Intrinsic grain contributions: grain dc-conductivity and dielectric relaxations due to local motions of electrons and lithium cations.

$Li_{3-2x}Co_xN$	**dc-conductivity**	**Li^+ motions (P5)**		**Electron motions (P6)**		**High-frequency Permittivity**
x						
	σ_g (S.m^{-1}) E_g (eV)	ν_i (Hz) E_i (eV) α_i	ν_{0i} (Hz) $\Delta\varepsilon_i$ β_i	ν_e (Hz) E_e (eV) α_e	ν_{0e} (Hz) $\Delta\varepsilon_e$ β_e	ε_{hf}
Li_3N						
	0.10	6.0×10^{8}	9.0×10^{11}			
x = 0.00*	0.19	0.19	3			9.3
		0.13	*0*			
$Li_{2.90}Co_{0.05}N$						
	0.20	6.0×10^{8}	9.0×10^{11}	3.0×10^{9}	3.0×10^{12}	
x = 0.05*	0.19	0.19	6.5	0.18	1.4	9.3
		0	*0*	*0.26*	*0*	
$Li_{2.76}Co_{0.12}N$						
	0.50	2.0×10^{8}	9.8×10^{11}	2.5×10^{9}	2.7×10^{12}	
x = 0.12*	0.21	0.21	28	0.18	3.7	11.1
		0.15	*0*	*0.10*	*0*	
$Li_{2.64}Co_{0.18}N$						
	1.30	5.0×10^{8}	1.1×10^{12}	3.7×10^{9}	3.7×10^{12}	
x = 0.18*	0.20	0.20	26	0.18	6.0	12.7
		0.03	*0*	*0.08*	*0*	
$Li_{2.50}Co_{0.25}N$						
	2.60	1.0×10^{10}	1.4×10^{13}	1.2×10^{9}	1.5×10^{13}	
x = 0.25*	0.21	0.19	4.6	0.25	18	14.5
		0.19	*0*	*0.08*	*0*	
$Li_{2.36}Co_{0.32}N$						
	0.56			2.3×10^{8}	6.0×10^{11}	
x = 0.32**	0.23			0.20	36	11
				0	*0.40*	
$Li_{2.22}Co_{0.39}N$						
	1.50			1.1×10^{9}	1.5×10^{12}	
x = 0.39**	0.20			0.19	26	16.5
				0.11	*0*	
$Li_{2.12}Co_{0.44}N$						
	3.00			4.5×10^{9}	4.6×10^{12}	
x = 0.44**	0.19			0.18	6.0	15
				0	*0*	

* Ionic conductors; ** Electronic conductors.

Figure Captions

Figure 1. (a) X-Ray diffraction patterns of the $Li_{3-2x}Co_xN$ samples; (b) Hexagonal structure ($P6_{/m}mm$) of $Li_{3-2x}Co_xN$ phases. Co^{+2} ions substitute Li^+ ions in the 1b site (in green), leading to the creation of an equivalent amount of vacancies □ in the 2c Li^+ site (in red). N^{3-} ions filled the 1a site.

Figure 2. Real parts of : a) conductivity σ' and b) permittivity ε' vs. frequency of $Li_{3-2x}Co_xN$ for different values of x at 300 K: x = 0, 0.05, 0.12, 0.25, 0.32, 0.39 and 0.44.

Figure 3. Nyquist plots of the complex resistivity (ρ" vs. ρ') at 300 K for the samples: a) $Li_{2.76}Co_{0.12}N$ (LCN2) and b) $Li_{2.22}Co_{0.39}N$ (LCN6). At the top of a) and b): entire plots from 60 to 10^{10} Hz and evidence of low-frequency contributions R1; at the bottom of a) and b): plots obtained after subtracting R1 and evidence of contributions R2. σ_g corresponds to grain dc-conductivity.

Figure 4. (a) Grain conductivity vs. molar cobalt content x: ionic (●) and electronic (●) conductivities.

Figure 5. Grain conductivity σ_g vs. inverse temperature 1/T for $Li_{3-2x}Co_xN$: a) ionic conductors (x = 0, 0.05, 0.12 and 0.25) and b) electronic conductors (x = 0.32, 0.39 and 0.44).

Figure 6. Nyquist plots of the imaginary part ε"(ω) vs. the real part ε'(ω) of the complex permittivity at 300 K for the sample $Li_{2.76}Co_{0.12}N$ (LCN2): a) entire plot from 40 to 10^{10} Hz: only the low frequency contribution P1 is visible; b) plot obtained upon subtracting the domain P1: evidence of the relaxation domains P2 and P3; c) plot obtained upon subtracting domains P2 and P3: evidence of the relaxation domain P4; d) plot obtained upon subtracting the domain P4: evidence of the relaxation domain P5; e) plot obtained upon subtracting the domain P5: evidence of the relaxation domain P6.

448 **Figure 7.** Nyquist plots of the imaginary part ε”(ω) vs. the real part ε’(ω) of the complex
449 permittivity at 300 K for the sample $Li_{2.36}Co_{0.32}N$ (LCN5): a) entire plot from 40 to 10^{10} Hz:
450 only the low frequency contribution P1 is visible; b) plot obtained upon subtracting the
451 domain P1: evidence of the relaxation domains P2 and P3; c) plot obtained upon subtracting
452 domains P2 and P3: evidence of the relaxation domain P4; d) plot obtained upon subtracting
453 the domain P4: evidence of the relaxation domain P6.

454 **Figure 8.** Nyquist plots of the imaginary part ε”(ω) vs. the real part ε’(ω) of the complex
455 permittivity at 300 K for the sample $Li_{2.22}Co_{0.39}N$ (LCN6): a) entire plot from 40 to 10^{10} Hz:
456 only the low frequency contribution P1 is visible; b) plot obtained upon subtracting the
457 domain P1: evidence of the relaxation domains P2 and P3; c) plot obtained upon subtracting
458 domains P2 and P3: evidence of the relaxation domain P4; d) plot obtained upon subtracting
459 the domain P4: evidence of the relaxation domain P6.

460 **Figure 9.** Relaxation frequencies as function of inverse temperature for: (a) x = 0.12 (Li^+
461 motions = ■ and electron motions = ■), (b) x = 0.25 (Li^+ motions = ■ and electron motions =
462 ■), (c) x = 0.44 (■), 0.39 (■) and 0.32 (■) (electron motions). (d) Relaxation frequencies of
463 lithium ions (■) and electrons (■) motions as function of x at 293 K. (e) Dielectric strength Δε
464 as function of x for relaxations due to ion (■) and electron motions (■) at 293 K

465 **Figure 10.** a) Comparison of the dielectric relaxation frequency ν_k (at 300 K) with $\sigma_g/2\pi\varepsilon_0\Delta\varepsilon_k$
466 which is the ratio the grain conductivity σ_g to the relaxation dielectric strength
467 $\Delta\varepsilon_k$ ($\alpha\tau$ 300 K) divided by the factor $2\pi\varepsilon_0 = 5.56\times10^{-11}$ $F.m^{-1}$ (*subscripts k = i and e*
468 *correspond to ionic and electronic motions, respectively*).

469 **Figure 11.** (a) Distribution of cobalt ions in crystal lattice perpendicular to c-axis for: (a) x =
470 0.18 and (b) x = 0.44; (c) Grain conductivity vs. molar cobalt content y = (2-x)x ionic where
471 (2-x) is the concentration of mobile $Li^+(2)$ cations and x the concentration of Li^+ vacancies on

472 2c sites. (d) Schematic 3D percolation of Li^+ conduction where each $Li^+(2)$ ion has 11
473 neighboring possible sites considering the transfers parallel to the c axis and to the (2c) plane.

474

(a)

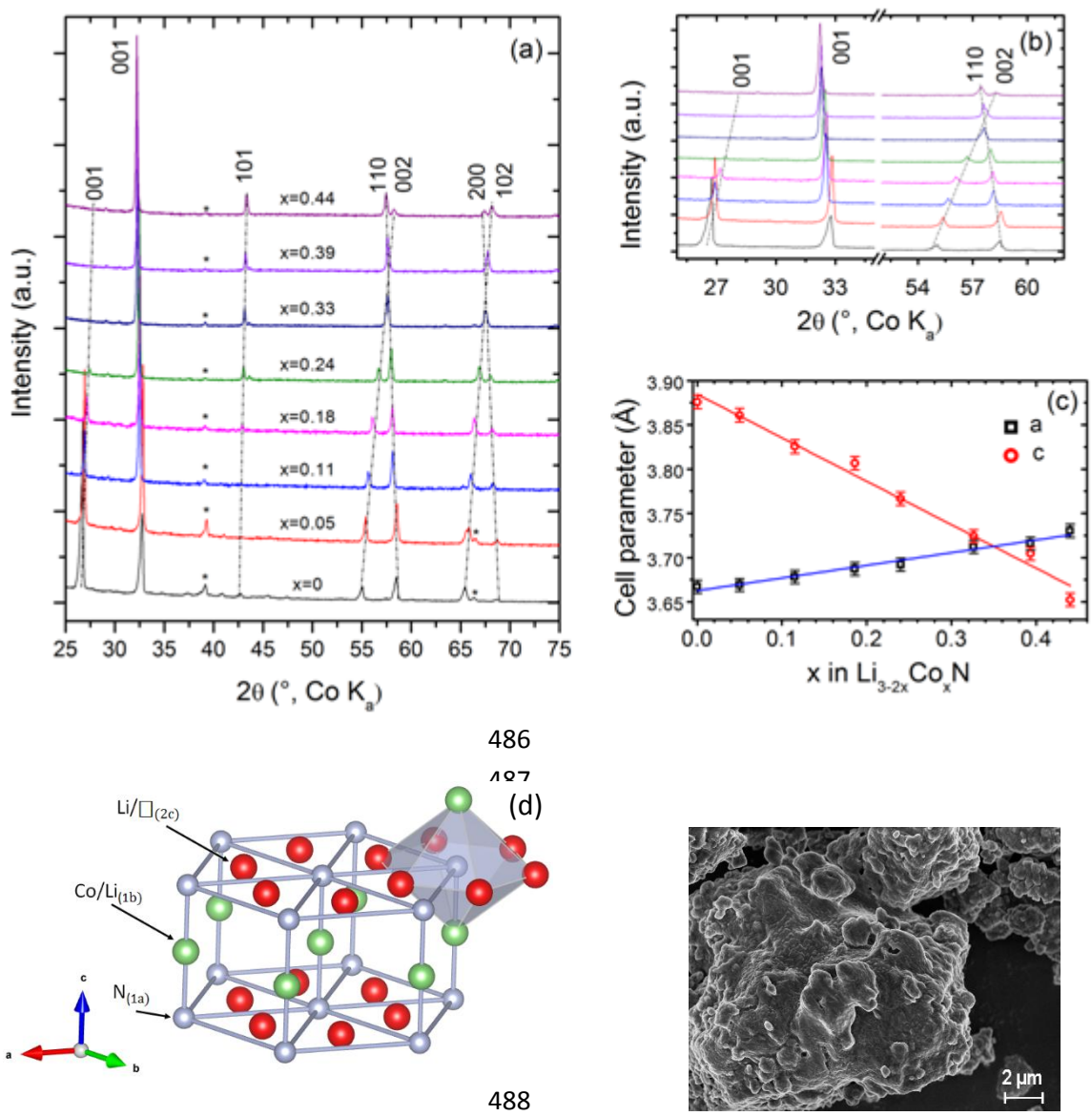
(a)
001
001
101
110
002
200
102
x=0.44
x=0.39
x=0.33
x=0.24
x=0.18
x=0.11
x=0.05
x=0
Intensity (a.u.)
2θ (°, Co K$_a$)
(b)
001
001
110
002
Intensity (a.u.)
2θ (°, Co K$_a$)
(c)
a
c
Cell parameter (Å)
x in Li$_{3-2x}$Co$_x$N
(d)
Li/□$_{(2c)}$
Co/Li$_{(1b)}$
N$_{(1a)}$
c
a
b
2 μm

Figure 1.

(a)

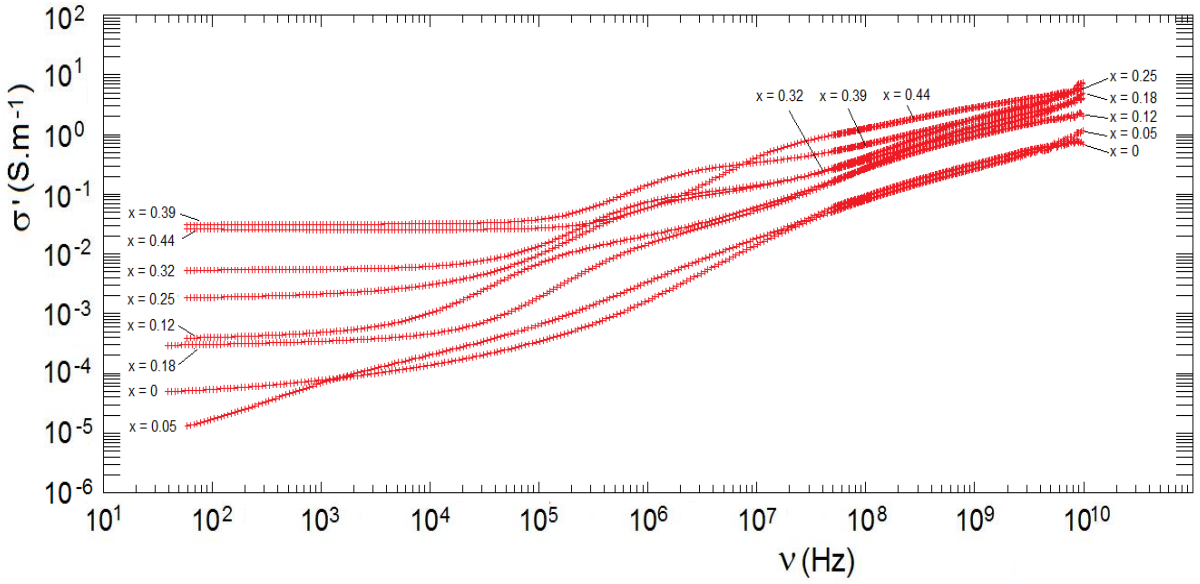
σ'(S.m-1)
ν (Hz)
x = 0.39
x = 0.44
x = 0.32
x = 0.25
x = 0.12
x = 0.18
x = 0
x = 0.05

(b)

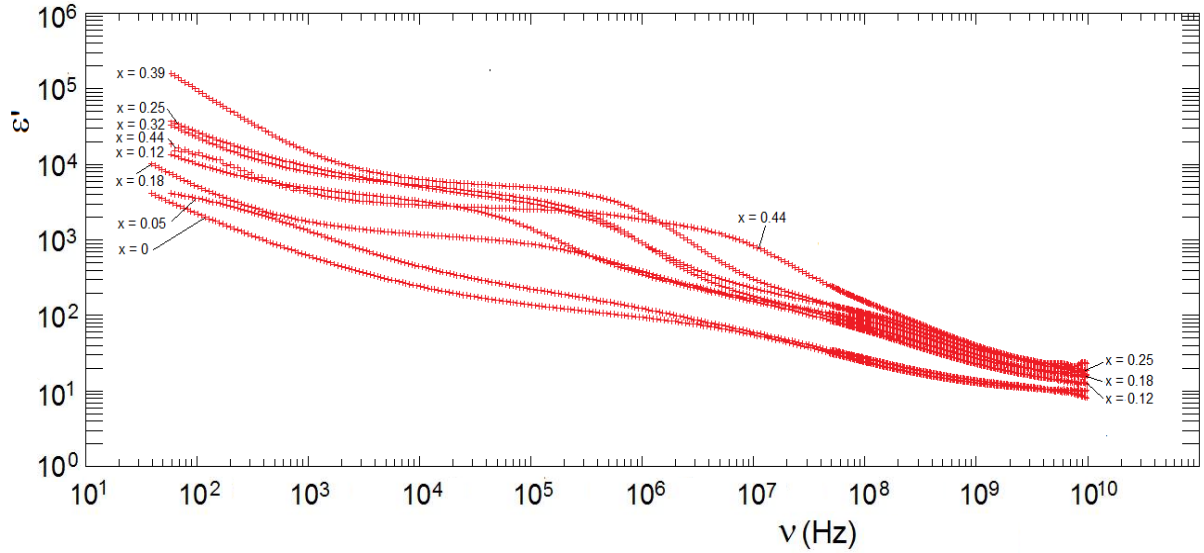
ε'
ν (Hz)
x = 0.39
x = 0.25
x = 0.32
x = 0.44
x = 0.12
x = 0.18
x = 0.05
x = 0

Figure 2

(a)

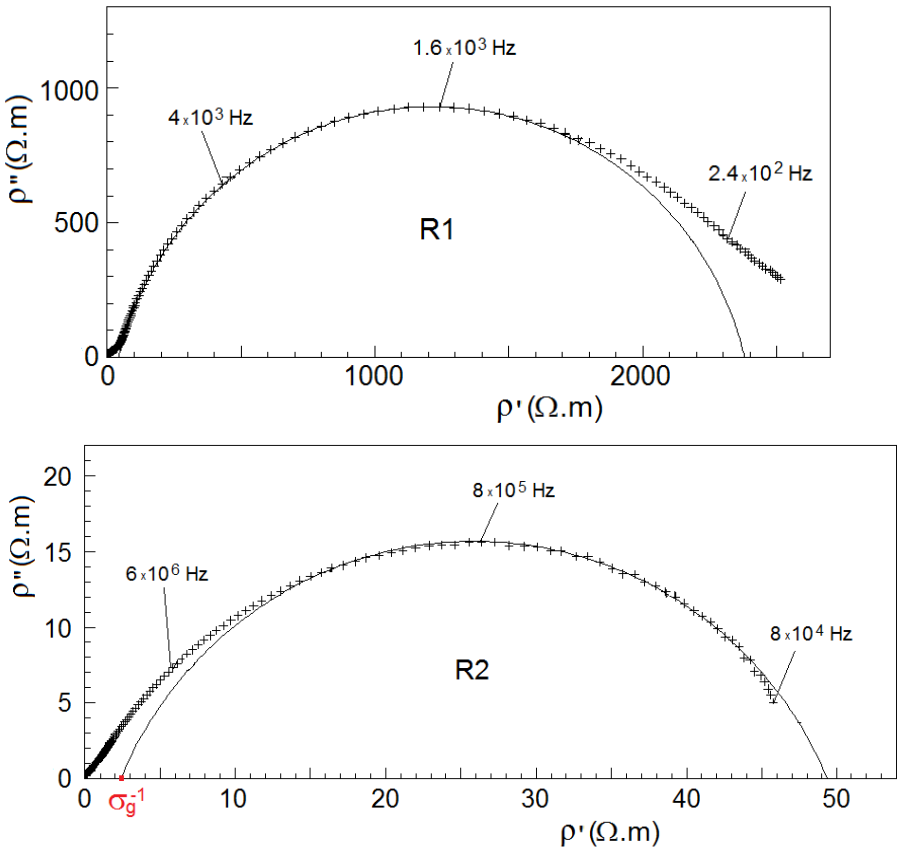
1.6x10³ Hz
4x10³ Hz
2.4x10² Hz
R1
ρ''(Ω.m)
ρ'(Ω.m)
8x10⁵ Hz
6x10⁶ Hz
8x10⁴ Hz
R2
σg⁻¹

(b)

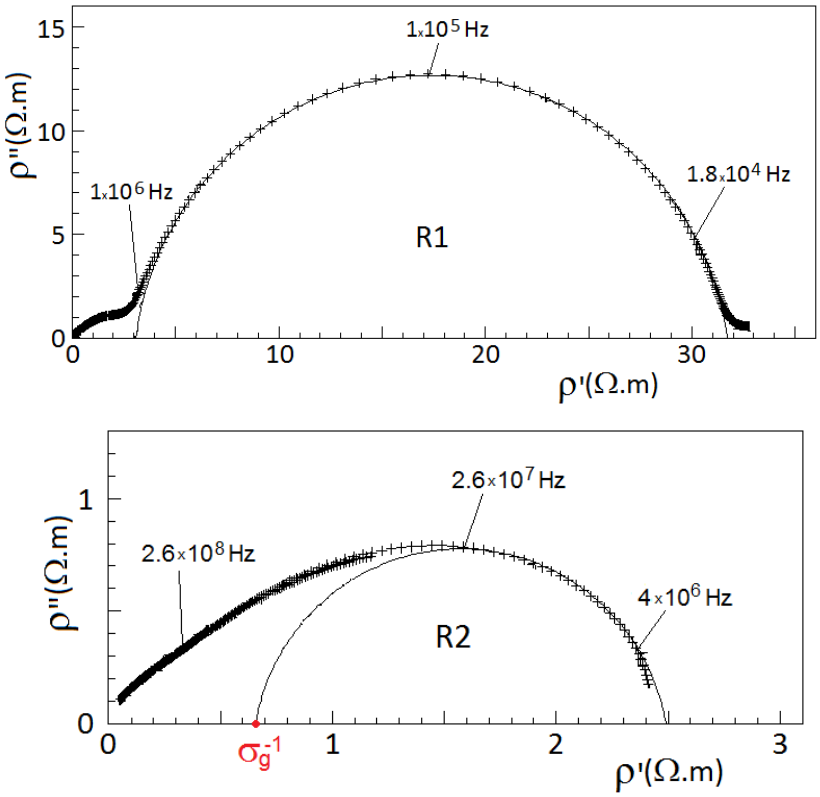
1x10⁵ Hz
1x10⁶ Hz
1.8x10⁴ Hz
R1
ρ''(Ω.m)
ρ'(Ω.m)
2.6x10⁷ Hz
2.6x10⁸ Hz
4x10⁶ Hz
R2
σg⁻¹

Figure 3.

(a)

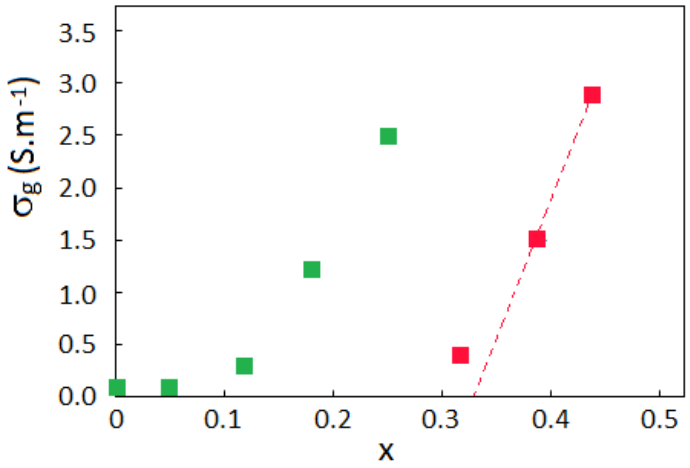

Figure 4.

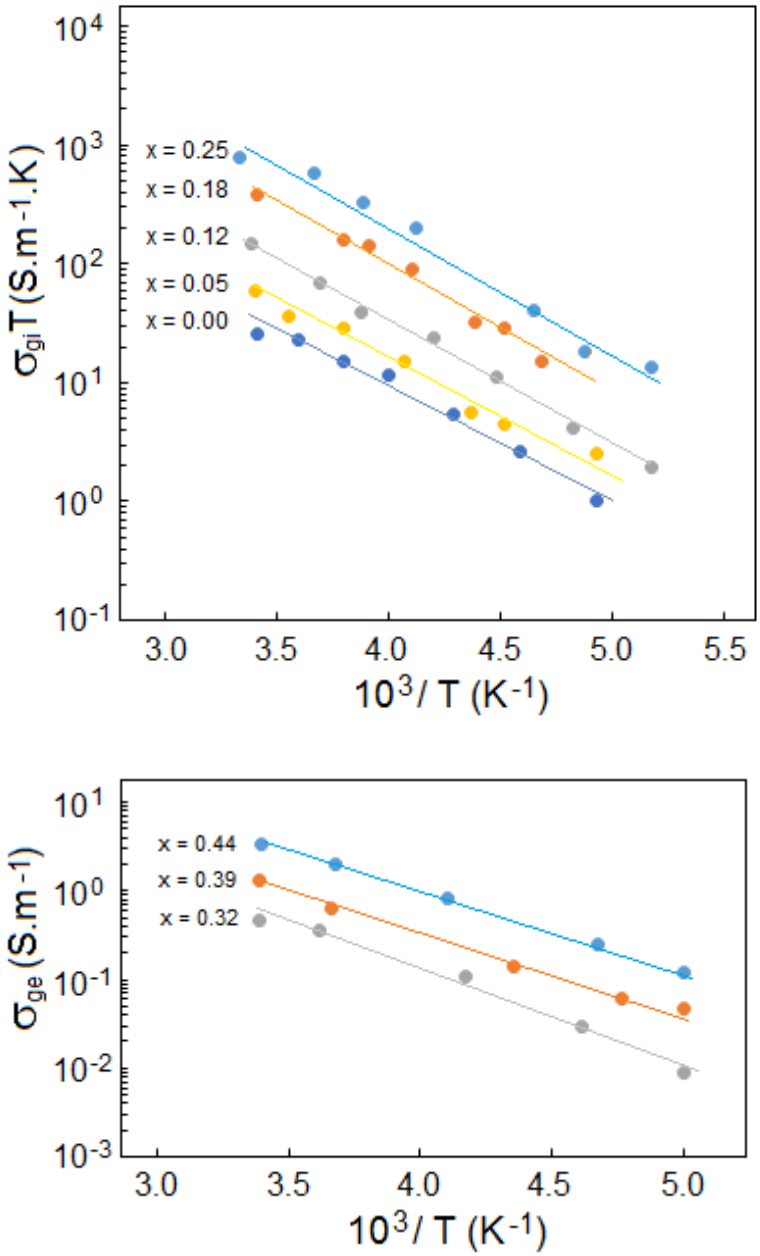
$\sigma_{gi}T$ (S.m^{-1}.K)
10^4
10^3
10^2
10^1
10^0
10^{-1}
x = 0.25
x = 0.18
x = 0.12
x = 0.05
x = 0.00
3.0
3.5
4.0
4.5
5.0
5.5
10^3/ T (K^{-1})
σ_{ge} (S.m^{-1})
10^1
10^0
10^{-1}
10^{-2}
10^{-3}
x = 0.44
x = 0.39
x = 0.32
3.0
3.5
4.0
4.5
5.0
10^3/ T (K^{-1})

Figure 5.

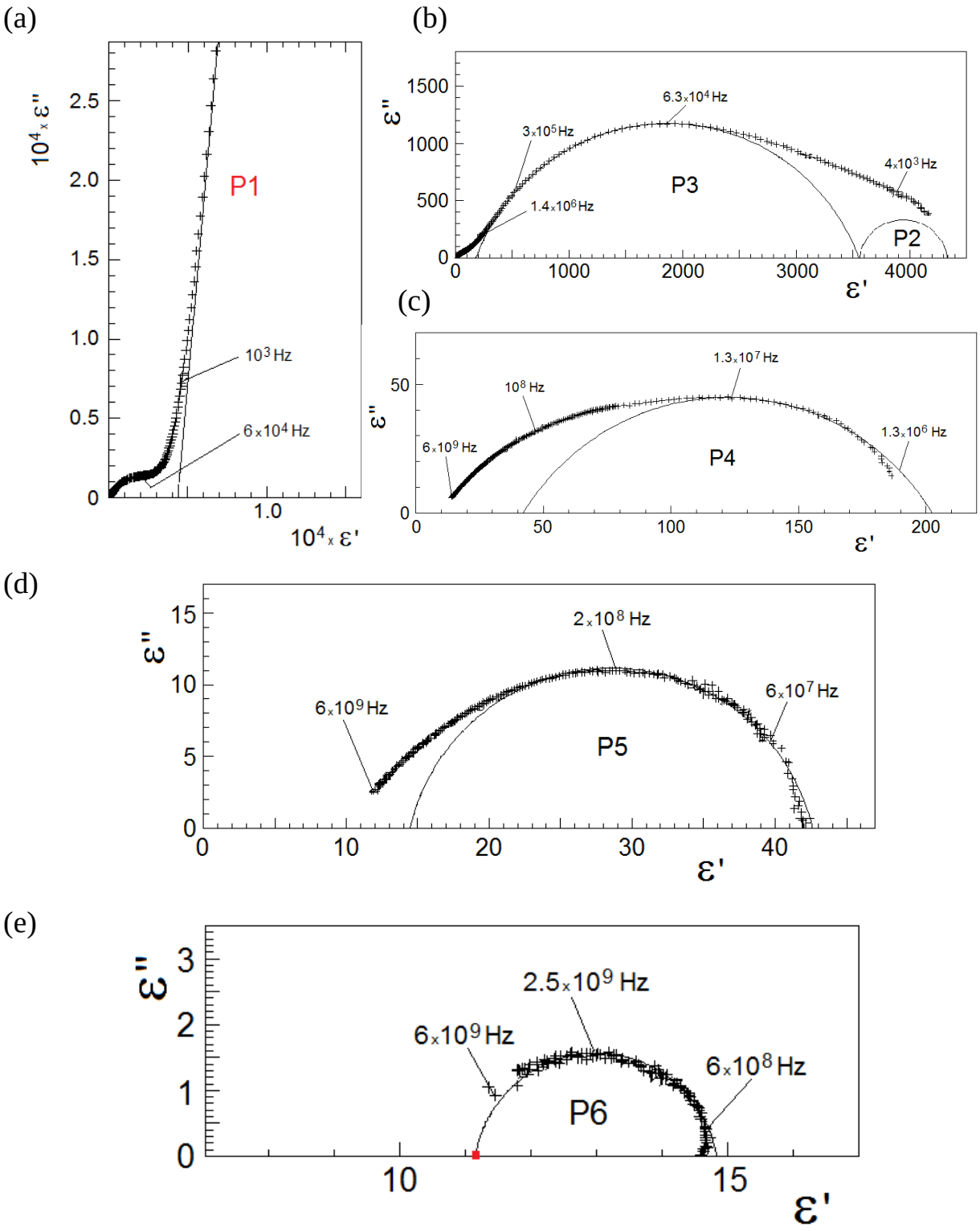
(a)
P1
10³ Hz
6x10⁴ Hz
10⁴x ε''
10⁴x ε'
(b)
6.3x10⁴ Hz
3x10⁵ Hz
4x10³ Hz
1.4x10⁶ Hz
P3
P2
ε''
ε'
(c)
1.3x10⁷ Hz
10⁸ Hz
6x10⁹ Hz
1.3x10⁶ Hz
P4
ε''
ε'
(d)
2x10⁸ Hz
6x10⁹ Hz
6x10⁷ Hz
P5
ε''
ε'
(e)
2.5x10⁹ Hz
6x10⁹ Hz
6x10⁸ Hz
P6
ε''
ε'

Figure 6.

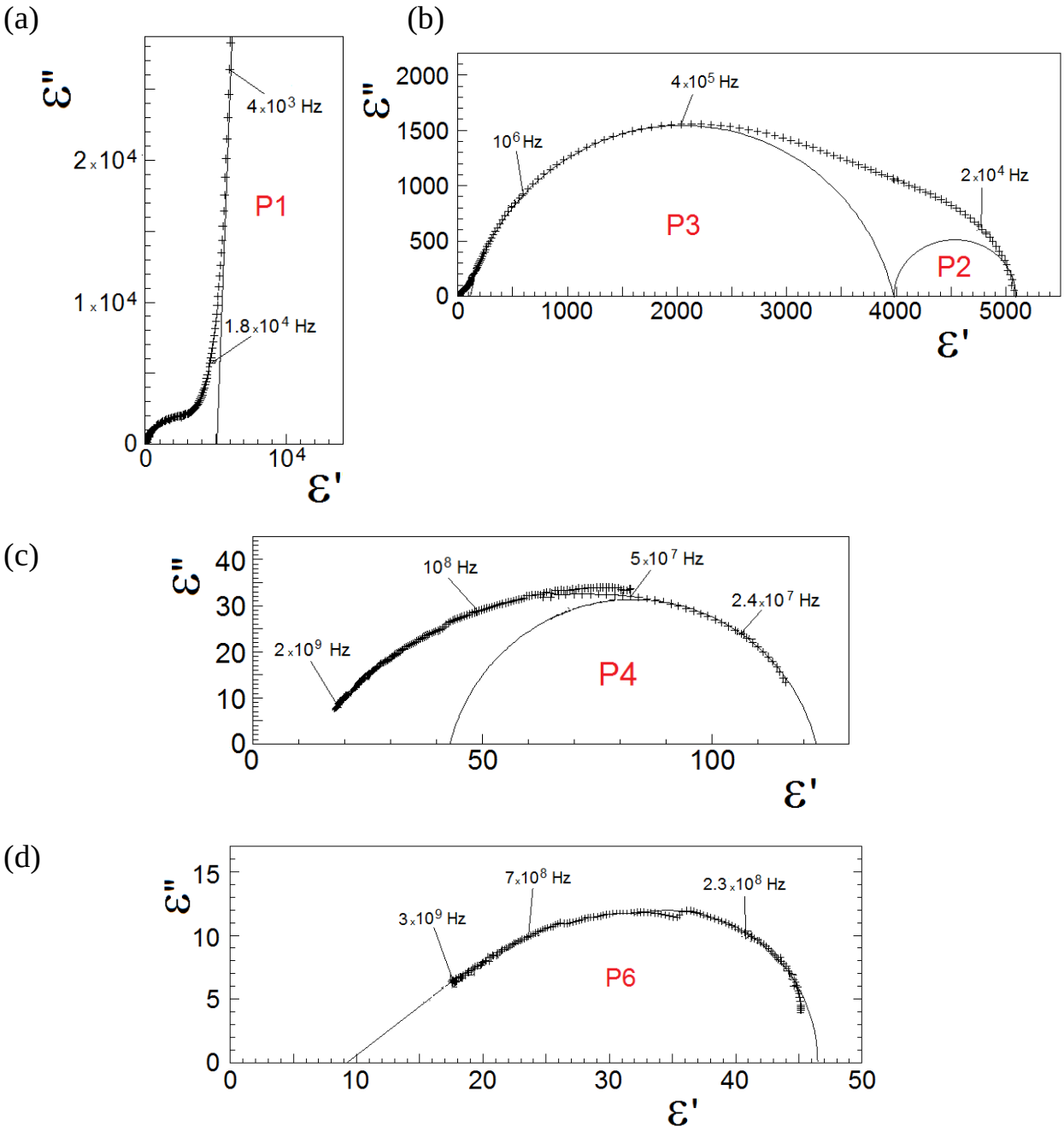
(a)
ε"
2×10^4
1×10^4
0
0
10^4
ε'
4×10^3 Hz
1.8×10^4 Hz
P1
(b)
ε"
2000
1500
1000
500
0
0
1000
2000
3000
4000
5000
ε'
4×10^5 Hz
10^6 Hz
2×10^4 Hz
P3
P2
(c)
ε"
40
30
20
10
0
0
50
100
ε'
10^8 Hz
5×10^7 Hz
2.4×10^7 Hz
2×10^9 Hz
P4
(d)
ε"
15
10
5
0
0
10
20
30
40
50
ε'
7×10^8 Hz
2.3×10^8 Hz
3×10^9 Hz
P6

Figure 7

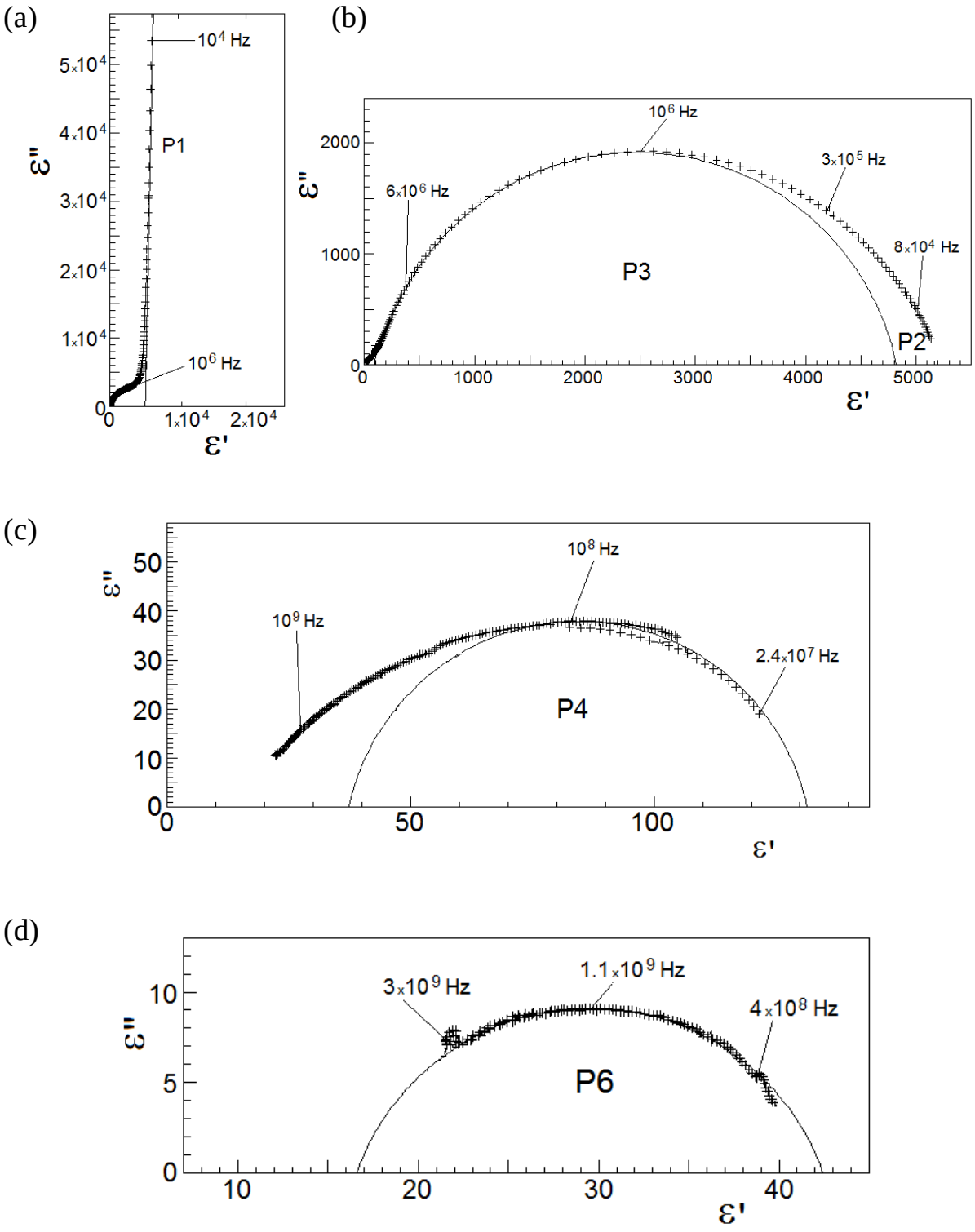
(a)
10⁴ Hz
P1
10⁶ Hz
ε''
ε'
(b)
10⁶ Hz
3x10⁵ Hz
6x10⁶ Hz
8x10⁴ Hz
P3
P2
ε''
ε'
(c)
10⁸ Hz
10⁹ Hz
2.4x10⁷ Hz
P4
ε''
ε'
(d)
1.1x10⁹ Hz
3x10⁹ Hz
4x10⁸ Hz
P6
ε''
ε'

Figure 8.

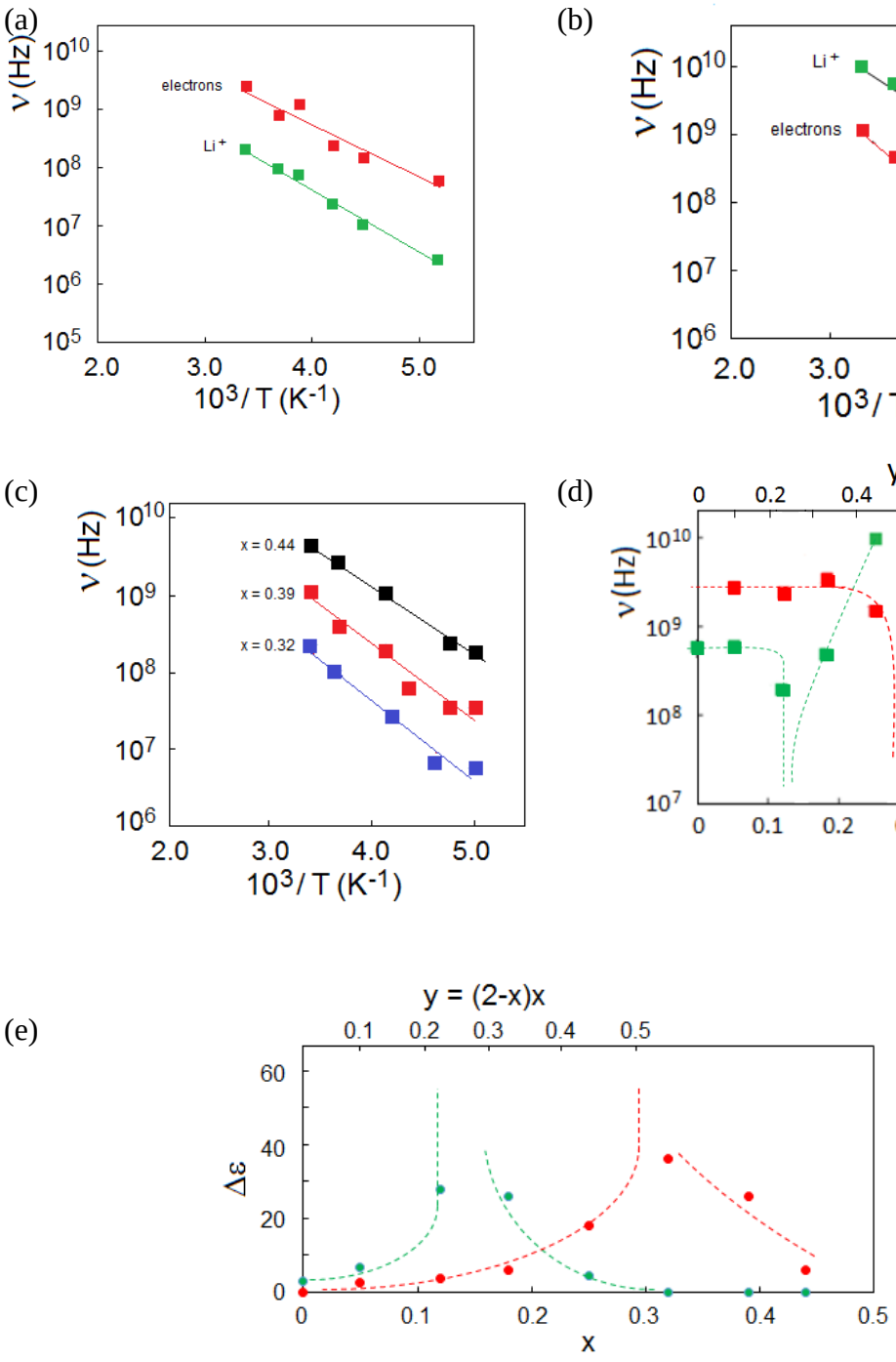
(a)
ν (Hz)
electrons
Li+
10^3/ T (K-1)
(b)
Li+
electrons
(c)
x = 0.44
x = 0.39
x = 0.32
(d)
y=(2-x)x
x
(e)
y = (2-x)x
Δε
x

Figure 9

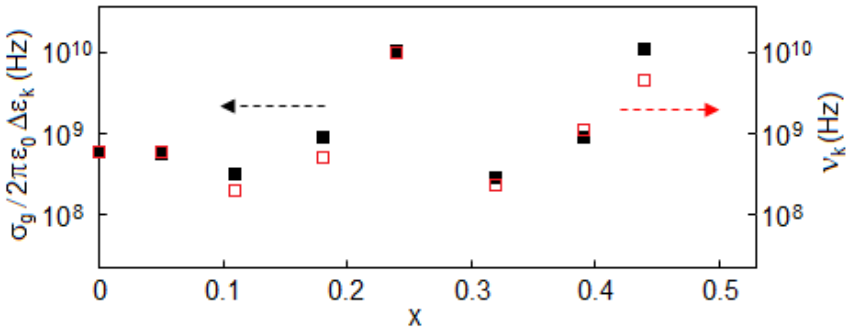
$\sigma_g / 2\pi\varepsilon_0\Delta\varepsilon_k$ (Hz)
10^{10}
10^9
10^8
ν_k (Hz)
0
0.1
0.2
0.3
0.4
0.5
x

Figure 10.

(a) (b)

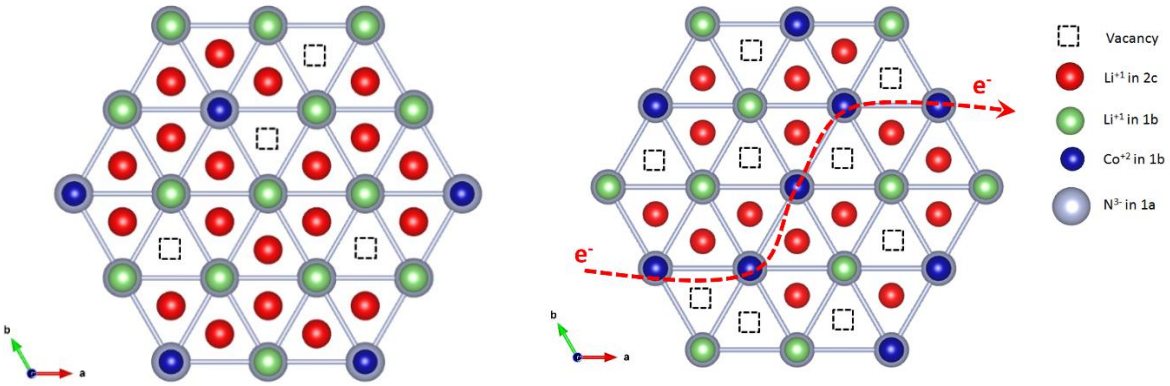

(c)

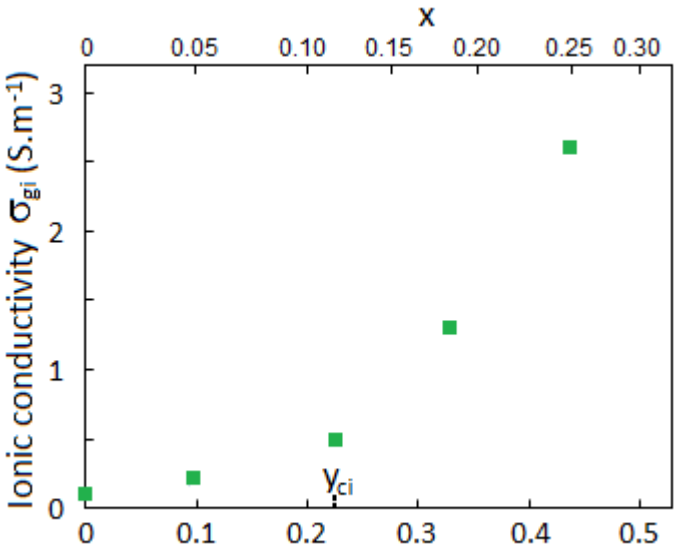

(d)

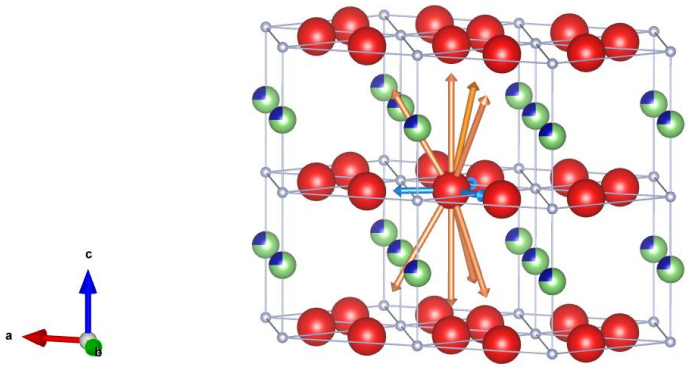

Figure 11.

726

References

[1] N. Tapia-Ruiz, M. Segalès, D. H. Gregory, *Coord. Chem. Rev.*, 2013, **257**,1978-2014.

[2] J. M. Cameron, R. W. Hughes, Y. Zhao, D. H. Gregory, *Chem. Soc. Rev.* 2011, **40**, 4099-4118

[3] D. C. S. Souza, V. Pralong, A. J. Jacobson, L. F. Nazar, *Science*, 2002, **296**, 2012-2015

[4] R. Alcantara, J. L. Tirado, J. C. Jumas, L. Montconduit, J. Olivier-Fourcade, *J. Power Sources*, 2002, **109**, 308-312

[5] R. A. Huggins, *J. Power Sources*, 1999, **81-82**, 13-19

[6] I. Rom, M. Wachtler, I. Papst, M. Schmied, J. O Besenhard, F. Hofer, M. Winter, *Solid State Ionics*, 2001, **143**, 329-336

[7] D. Muller-Bouvet, N. Emery, N. Tassali, E. Panabière, S. Bach, O. Crosnier, T. Brousse, C. Cénac-Morthe, A. Michalowicz, J.P. Pereira-Ramos, *Phys. Chem. Chem. Phys*, 2017, **19**, 27204

[8] N. Emery, M.T. Sougrati, E. Panabière, S. Bach, B. Fraisse, J.C. Jumas, J.P. Pereira-Ramos, P. Willmann, *J. All. Comp.*, 2017, **696**, 971-979

[9] E. Panabière, N. Emery, S. Bach, J.P. Pereira-Ramos, P. Willmann, *Electrochim. Acta*, 2013, **97**, 393-397

[10] E. Panabière, N. Emery, S. Bach, J.P. Pereira-Ramos, P. Willmann, *J. Alloys Comp.*, 2016, **663**, 624-630

[11] M. Nishijima, N. Tadokoro, Y. Takeda, N. Imanishi, O. Yamamoto, *J. Elecrtrochem. Soc.*, 1994, **141**, 2966-2971

[12] J. Cabana, C.M. Ionica-Bousquet, C.P. Grey, M.R. Palacin, *Electrochem. Comm.*, 2010, **12**, 315-318

[13] T. Shodai, S. Okada, S. Tobishima, J. Yamaki, *J. Power Sources*, 1997, **68**, 515-518.

[14] M. Nishijima, T. Kagohashi, M. Imanishi, Y. Takeda, O. Yamamoto, S. Kondo, *Solid State Ionics*, 1996, **83**, 107-111

[15] T. Cavoué, N. Emery, N. Umirov, S. Bach, P. Berger, Z. Bakenov, C. Cénac-Morthe, J.P. Pereira-Ramos, *inorg. Chem.*, 2017, **56**, 13815-13821

[16] J.B. Ducros, S. Bach, J.P. Pereira-Ramos, P. Willmann, *J. Power Sources*, 2008, **175**, 517-525.

[17] J. B. Ducros, S. Bach, J. P. Pereira-Ramos, P. Willmann, *Electrochim. Acta.*, 2015, **167**, 20-24

[18] J.B. Ducros, S. Bach, J.P. Pereira-Ramos, P. Willmann, *Electrochim. Acta*, 2007, **52**, 7035-7041

[19] W. Sachsze, R. Juza, *Z. Anorg. Chem.*, 1949, **259**, 278-290

[20] S. Berthumeyrie, J.-C. Badot, J.-P. Pereira-Ramos, O. Dubrunfaut, S. Bach, Ph. Vermaut, *J. Phys. Chem. C*, 2010, **114**, 19803.

[21] J-C. Badot, E. Ligneel, O. Dubrunfaut, J. Gaubicher, D. Guyomard, B. Lestriez, *Phys. Chem. Chem. Phys.*, 2012, **14**, 9500–9510

[22] K. A. Seid, J. C. Badot, O. Dubrunfaut, S. Levasseur, D. Guyomard, B. Lestriez, *J. Mater. Chem.*, 2012, **22**, 2641- 2649

[23] K. A. Seid, J. C. Badot, O. Dubrunfaut, S. Levasseur, D. Guyomard, B. Lestriez, *J. Mater. Chem.*, 2012, **22**, 24057-24066

[24] U. Von Alpen, A. Rabenau, G. H. Talat, *Appl. Phys. Lett.*, 1977, **30**, 621-623
[25] B. A. Boukamp, R. A. Huggins, *Phys. Lett.*, 1976, **58A**, 231-233
[26] J.C. Badot, E. Ligneel, O. Dubrunfaut, D. Guyomard, B. Lestriez, *Adv. Funct. Mater*. 2009, **19**, 2749-2758
[27] T. Asai, K. Nishida, S. Kawai, Mat. Res. Bull., 1984, **19**, 1377-1381
[28] D.H. Gregory, P.M O'Meara, A.G. Gordon, J.P. Hodges, S. Short, J.D. Jorgensen, J.D, *Chem. Mater*., 2002, **14**, 2063-2070
[29] E. Panabière, N. Emery, S. Bach, J.P. Pereira-Ramos, P. Willmann, *Corr. Sci*., 2012, **58**, 237-241
[30] E. Barsoukov, J.R. Macdonald, Impedance Spectroscopy: Theory, Experiment and Applications, Third Edition, 2018, John Wiley & Sons, Inc.
[31] I. Ibach, H. Lüth, Solid State Physics 3rd edition, Springer ISSN 1439-2674 or R.B. Heslop, K. Jones, Inorganic Chemistry, Elsevier 1976).
[32]O. Madelung, Introduction to Solid State Physics, Springer Verlag, Berlin, 1981.
[33] K.A. Seid *et al*, *Phys. Chem. Chem. Phys.*, 2014, **15**, 19790-19798
[34] H.Namikawa, *J. Non-Cryst. Solids*, 1975, **18**, 173-195
[35] G. Garcia-Belmonte, J. Bisquert, *J. Chem. Phys.*, 2005, **123**, 074504/1-4
[36] A.L. Efros, B.I. Shklovskii. *Phys. stat. sol. (b)*, 1976, **76**, 475-485
[37] D. Wilkinson, J.S. Langer, P. N. Sen, *Phys. Rev. B*, 1983, **28**, 1081-1087
[38] D.M.Grannan, J.C. Garland, D.B. Tanner, *Phys. Rev. Lett.* 1981,**46**, 375-378
[39] Y.C. Li, R.K.Y.Li, S.C. Tjong, *J. Nanomater.*, 2010, 261748/1-10 doi: 10.1155/2010/261748.
[40] S. Kirkpatrick, *Rev. Mod. Phys.*, 1973, **45**, 574-588
[41] L. Turban, *J. Phys. C: Solid State Phys.*, 1978, **11**, 449-459
[42] D.J. Bergman, Y. Imri, *Phys. Rev. Lett.*, 1977, **39**, 1222-1225
[43] J. P. Calame, *J. Appl. Phys.*, 2003, **94**, 5945-5957
[44] H. Schulz, K.H. Thiemann, Acta cryst A, 1979, **35**, 309-314
[45] J. P. Clerc, G. Giraud, J.M. Laugier, J.M. Luck, J. M. *Adv. Phys*. 1990, **39**, 191–309